doi:10.1038/nature25436

A clumpy and anisotropic galaxy halo at redshift 1 from gravitational-arc tomography

Sebastian Lopez[1], Nicolas Tejos[2], Cédric Ledoux[3], L. Felipe Barrientos[4], Keren Sharon[5], Jane R. Rigby[6], Michael D. Gladders[7,8], Matthew B. Bayliss[9] & Ismael Pessa[4]

Every star-forming galaxy has a halo of metal-enriched gas that extends out to at least 100 kiloparsecs[1–3], as revealed by the absorption lines that this gas imprints on the spectra of background quasars[4]. However, quasars are sparse and typically probe only one narrow beam of emission through the intervening galaxy. Close quasar pairs[5–7] and gravitationally lensed quasars[8–11] have been used to circumvent this inherently one-dimensional technique, but these objects are rare and the structure of the circumgalactic medium remains poorly constrained. As a result, our understanding of the physical processes that drive the recycling of baryons across the lifetime of a galaxy is limited[12,13]. Here we report integral-field (tomographic) spectroscopy of an extended background source—a bright, giant gravitational arc. We can thus coherently map the spatial and kinematic distribution of Mg II absorption—a standard tracer of enriched gas—in an intervening galaxy system at redshift 0.98 (around 8 billion years ago). Our gravitational-arc tomography unveils a clumpy medium in which the absorption strength decreases with increasing distance from the galaxy system, in good agreement with results for quasars. Furthermore, we find strong evidence that the gas is not distributed isotropically. Interestingly, we detect little kinematic variation over a projected area of approximately 600 square kiloparsecs, with all line-of-sight velocities confined to within a few tens of kilometres per second of each other. These results suggest that the detected absorption originates from entrained recycled material, rather than in a galactic outflow.

We use the Multi Unit Spectroscopic Explorer (MUSE)[14] mounted on the European Southern Observatory Very Large Telescope to observe the 38″-long gravitational arc RCSGA 032727−132623 (ref. 15). This arc results from a lensed galaxy at redshift 1.70, which is highly magnified and stretched by a massive galaxy cluster at redshift 0.56 (Fig. 1). With a *g*-band magnitude of 19.15, it is among the brightest known arcs[16] and has a high surface brightness across a large area on the sky[17]. Magellan/MagE spectroscopy[18] of its brightest knot reveals the presence of a strong Mg II absorption system at redshift $z_{abs} = 0.98$, and we set out to map this absorption along the entire arc.

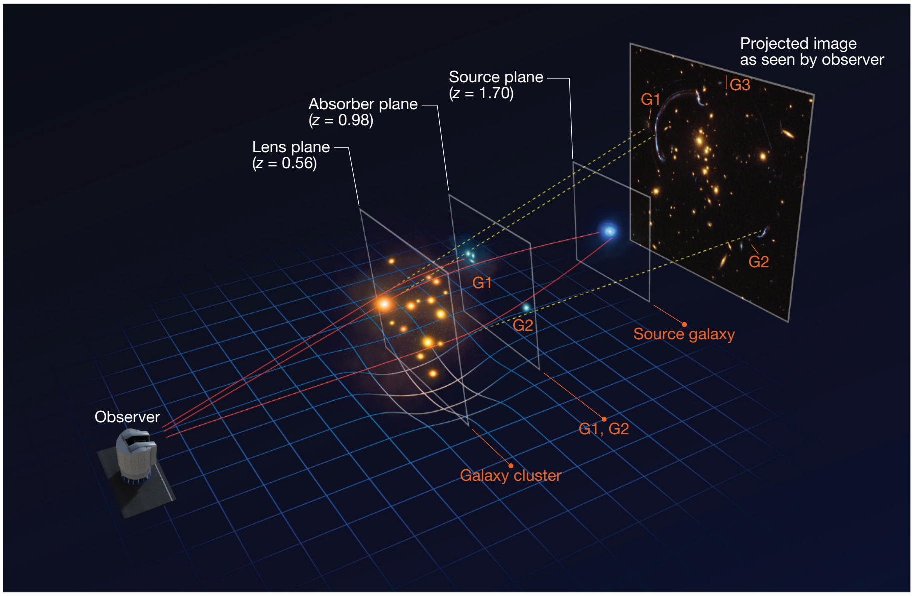

Figure 1 | Illustration of the lens geometry of the arc and the absorber in RCSGA 032727−132623. Light from the $z = 1.70$ background source galaxy ('source plane') is deflected and magnified (red lines) by an intervening galaxy cluster at $z = 0.56$ (ref. 15; 'lens plane') to form the bright giant arc that is seen projected (yellow dashed lines) onto the right-most panel ('image plane'). As the light crosses the $z_{abs} = 0.98$ 'absorber plane', some of it is absorbed by Mg II in the gas that surrounds an absorbing galaxy that lies close to the arc in projection. Three candidates for such galaxies are detected at this redshift, marked 'G1', 'G2' and 'G3' in the image plane. This work deals with G1 and G2 (also indicated in the absorber plane), which probe the closest projected distances to the arc. Image produced by Carlos Polanco.

[1]Departamento de Astronomía, Universidad de Chile, Casilla 36-D, Santiago, Chile. [2]Instituto de Física, Pontificia Universidad Católica de Valparaíso, Casilla 4059, Valparaíso, Chile. [3]European Southern Observatory, Alonso de Córdova 3107, Casilla 19001, Vitacura 19, Santiago, Chile. [4]Instituto de Astrofísica, Pontificia Universidad Católica de Chile, Vicuña Mackenna 4860, Santiago, Chile. [5]Department of Astronomy, University of Michigan, 500 Church Street, Ann Arbor, Michigan 48109, USA. [6]Observational Cosmology Laboratory, NASA Goddard Space Flight Center, 8800 Greenbelt Road, Greenbelt, Maryland 20771, USA. [7]Department of Astronomy and Astrophysics, University of Chicago, 5640 South Ellis Avenue, Chicago, Illinois 60637, USA. [8]Kavli Institute for Cosmological Physics, University of Chicago, 5640 South Ellis Avenue, Chicago, Illinois 60637, USA. [9]Kavli Institute for Astrophysics and Space Research, Massachusetts Institute of Technology, 77 Massachusetts Avenue, Cambridge, Massachusetts 02139, USA.

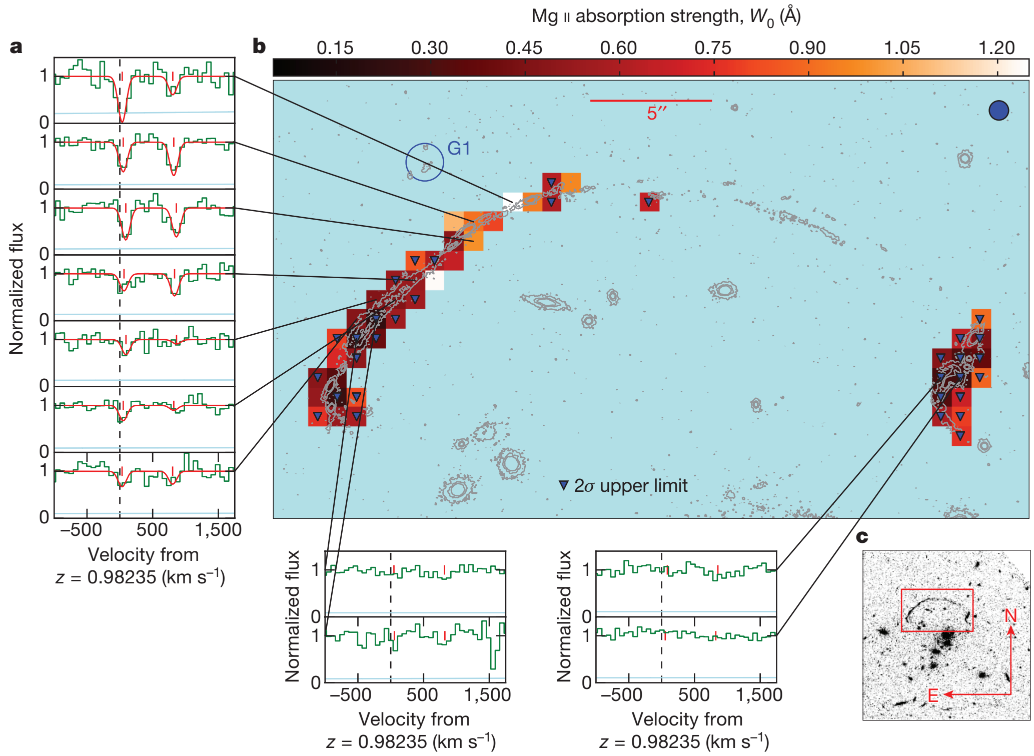

Figure 2 | Map of Mg II absorption strengths at approximately 4-kpc resolution. **a**, Representative sample of MUSE spectra of the Mg II $\lambda = 2{,}796$ Å, $\lambda = 2{,}803$ Å absorption doublets (green histograms) and corresponding Gaussian fits and line centroids (red lines and red ticks, respectively) in velocity space with respect to $z_{G1} = 0.98235$. Panels without fits correspond to non-detections. The black lines indicate the corresponding positions on the arc. **b**, $0.51' \times 0.27'$ inset of the $1' \times 1'$ MUSE field centred in the northeastern part of the arc. The colour scale indicates Mg II $\lambda = 2{,}796$ Å rest-frame absorption strengths obtained from the Gaussian fits. A total of 56 positions were selected to have a continuum signal-to-noise ratio above 3 at the expected Mg II lines (50 shown here), of which 18 have significant detections (see Extended Data Fig. 2, Extended Data Tables 1 and 2 and Methods). Non-detections are indicated by blue downward arrows. The candidate absorber G1 is indicated by the blue circle (to the northeast). For reference, we overlay arc and galaxy contours (grey lines) at 840 nm from HST data (GO programme 12267). Each independent spatial element (spaxel) is 0.8″ wide, equivalent to four MUSE unbinned spaxels and of similar size to the seeing (indicated by the blue circle in the top right). This grid is defined in the image plane; the actual spatial resolution varies across the absorber plane from about 4 kpc at the eastern side of the arc to about 2 kpc at the western side. Likewise, the 5″ scalebar corresponds to a range of roughly 24–12 kpc in the absorber plane, depending on position (see Extended Data Fig. 3 for a de-lensed image). **c**, Entire MUSE field of view indicating the location of the Mg II map shown in **b**.

In Fig. 2 we show a MUSE map of the $z_{abs} = 0.98$ Mg II absorption strength at different positions along RCSGA 032727−132623. In the absorber plane, the arc positions span projected physical distances ('impact parameters'; see Methods) of approximately 15–90 kpc to the absorbing galaxy system ('G1'; indicated by the blue circle). G1 is our primary absorber candidate of the three [O II] detections at redshift 0.98 (G1, G2 and G3; Methods) and deserves special attention. Hubble Space Telescope (HST) continuum images resolve this system into three irregular galaxies, G1-A, G1-B and G1-C, which all have blue $B - I$ colours. From the HST photometry we estimate that these galaxies have low luminosities (less than about 5% of L^*, the characteristic luminosity of galaxies) and consequently low stellar masses compared to quasar absorbers[3]. Such stellar masses suggest total halo masses of around 10^{11} solar masses ($M_\odot$), which in turn imply virial radii of the dark-matter haloes of approximately 90 kpc (Methods). In addition, from the [O II] $\lambda = 3{,}726$ Å, $\lambda = 3{,}729$ Å emission doublets, where λ is the wavelength, we estimate the star-formation rates of the G1 galaxies to be less than about $0.2 M_\odot$ yr^{-1}. We use the [O II] velocities to define a 'systemic' redshift for G1 of $z_{G1} = 0.98235$.

Four key features are readily evident from Fig. 2: (a) Mg II is detected from about 15 kpc out to about 45 kpc to the south of G1, but is not detected further than approximately 80 kpc to the west (another arc knot in the south, not shown in Fig. 2, also has sensitive non-detections; see below); (b) the absorption strength is not uniform, indicating a clumpy medium on 4-kpc scales down to our detection limit of approximately 0.4 Å; (c) the line centroids vary little (within one spectral pixel, or about 50 km s^{-1}) all across the arc; and (d) most of the doublet ratios appear to be saturated, indicating possible partial covering of the background source (Methods).

In Fig. 3 we show that the absorption strength decreases with impact parameter, in broad agreement with the quasar statistics[3], but that the scatter is smaller than in the quasar data[2,3]. The latter is probably a consequence of partial covering, which would skew down the arc measurements (Methods); however, the heterogeneity of the compiled quasar–galaxy sample may also have a role[3,19], because the intervening galaxies encompass a wide range of masses, luminosities and orientations. That is to say, we compare averages over different areas in a single galaxy (probed by the arc) with an average over many distinct galaxies (probed by quasars).

From quasar lens statistics[8,20] we know that transverse structure is detected on similar scales as probed by our 4-kpc, seeing-limited resolution, and below. This indicates that the metals traced by Mg II are concentrated in small clouds that we do not resolve here, but are spatially distributed in such a way as to produce the gradient that we observe. Therefore, our data do not probe individual cloud sizes but rather their coherence length. Some stringent non-detections (Fig. 3) re-enforce the notion of clumpiness on kiloparsec scales.

The tomographic technique that we use enables us to scan the velocity field of the absorbing gas profusely in a single high-redshift halo[10]. Figure 4 displays absorption velocities and emission velocities of G1-A, G1-B and G1-C as a function of impact parameter. The first outstanding feature in this figure is that all absorption velocities lie

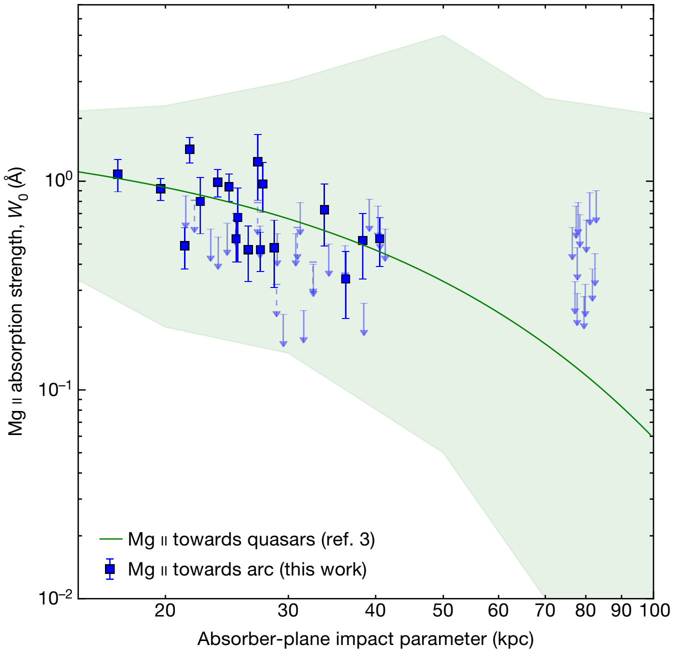

Figure 3 | Mg II absorption strength versus impact parameter. Squares correspond to detections and arrows to 2σ upper limits for the arc. Error bars correspond to the $\pm1\sigma$ uncertainty in the absorption strength measurement. All impact parameters are measured to G1 (northeast part of the arc), except for the six upper limits marked with dashed lines, which correspond to G2 (south). The zero-points are given by the centres of the blue circles in Fig. 2 and Extended Data Fig. 2. The green line is the fit to a sample of 182 quasar-absorption systems[3] and the shaded area indicates the full scatter in that sample. Uncertainties in the impact parameters are less than about 5%. 'Mg II towards quasars' and 'Mg II towards arc' in the legend indicates data obtained using quasars or the arc as background sources, respectively.

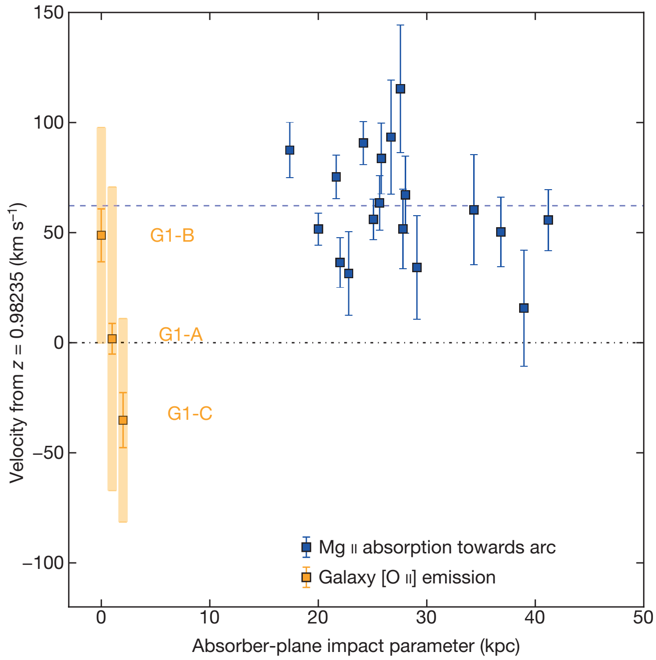

Figure 4 | Gas kinematics. Blue symbols correspond to the Mg II $\lambda = 2{,}796$ Å, $\lambda = 2{,}803$ Å absorption-line velocities of the arc and orange symbols to the [O II] $\lambda = 3{,}726$ Å and $\lambda = 3{,}729$ Å emission-line velocities of G1 (shifted in the x axis for clarity). The blue dashed line indicates the average absorption velocity. The zero-point velocity corresponds to the systemic redshift $z_{G1} = 0.98235$. Error bars correspond to the $\pm1\sigma$ uncertainty in the velocities. The envelopes around the emission-line measurements (orange shading) indicate the full-width at half-maximum (FWHM) velocity dispersion derived from the [O II] fits. Uncertainties in the impact parameters are less than about 5%.

redward of z_{G1}, at $+62$ km s^{-1}, although none of them substantially exceeds any of the velocity dispersions of the galaxies. Second, there is little overall variation in absorption velocity along the arc (approximately 24 km s^{-1}), even less than within the galaxy system itself, but this variation extends out to 40 kpc, a distance 10 times larger than the projected separations between the G1 galaxies. Along with a clumpy medium revealed by the map of absorption strengths, this kinematically quiet behaviour places strong constraints on the geometry and dynamics of this system.

Assuming saturation, the absorption strengths are a measure of the velocity spread of individual clouds[21] (not resolved by our data) and possible partial covering (see Methods). Therefore, most of our detections would correspond to velocity spreads of less than about 108 km s^{-1} along the sightlines, the equivalent of a 1-Å absorption line. Interestingly, we find lower scatter in the transverse direction. Taken together, these findings would indicate gas clouds with internal velocity dispersions that dominate over bulk motions. For the impact parameters and halo mass probed here, these velocities resemble those determined at higher spectral resolution in low-redshift systems[22,23], which appear well within the escape velocity and virial radius of the halo.

Our observations do not support a spherical geometry[24,25]. The Mg II gas does not seem to be distributed isotropically around G1; if this were the case, similar absorption would occur at both sides of the line connecting G1 and its closest arc position, which we do not see. Instead, there are more non-detections on the southern side. G2 (Methods) is also a good example of this situation: no Mg II is detected in six positions at roughly 20–30 kpc to sensitive limits, whereas four are expected if G2 followed the trend shown in Fig. 3 isotropically. Furthermore, assuming the observed Mg II to be related to only one of the G1 galaxies, then only one of the four galaxies (including G2) presents detectable absorption, which leads to a rough covering fraction of about 25% within 40 kpc. This interpretation assumes that the G1 galaxies are distinct objects and not part of a large disk of gas and dust (Methods). Therefore, in line with quasar-absorber observations[26,27], our arc observations strongly suggest that the absorbing gas is anisotropic, with wide (possibly around 90°) opening angles[28].

Our data also enable us to compute gas covering fractions in an alternative fashion, namely directly from our 'hits and misses' statistics around G1 only (Methods). Assuming anisotropy, we probe here the preferential G1 direction that shows absorption; therefore, our covering fraction estimate should lie above that of quasar absorbers, because those surveys probe random quasar–galaxy orientations. Interestingly, our prediction is fulfilled in comparison with galaxy-selected quasar absorbers[2], which we regard to be unbiased: the covering fraction towards the arc is indeed larger than towards the quasars in that sample (Methods). Conversely, a comparison with more heterogeneous samples that include Mg II-selected galaxies[3] yields smaller covering fractions towards the arc than towards the quasars. This suggests possible selection biases in the latter samples, because by construction they favour galaxy orientations that produce absorption[19].

At low redshift there is observational evidence[23,29] that the circumgalactic medium of star-forming galaxies is driven by the interplay between major-axis entraining gas (pristine or recycled) and enriched outflows aligned with the minor axis. Although this picture is also consistent with most recent simulations and ΛCDM predictions[30], it remains to be confirmed, particularly at high redshift. Here we deal with dwarf galaxies at redshift 1, which are still able to eject metals[12] out to one virial radius, beyond which the metal flux is expected to have decreased markedly[30]. The Mg II detections that we report occur well within the virial radius and therefore could have originated from any of the G1 galaxies (but given the relatively quiet velocity field, most probably from only one of them). In addition, the gas is metal-enriched (including in Fe II; see Methods) and patchy (perhaps revealing a multi-phase medium), which is suggestive of recycled gas either outflowing from or bound to one of the individual G1 haloes. The outflow scenario requires outflow speeds[6,26] in excess of the offsets between the velocities of the galaxies and the gas observed here (Fig. 4). This suggests that the Mg II is more likely to be correlated with entrained gas in the extended halo of G1-B (closer in velocity), or even G1-A, in which case the absorption velocity offset would resemble the one-sided velocity offsets seen at low redshift[22,23].

The gravitational-arc tomography presented here appears to probe the gaseous extension of a galaxy halo in formation, at distances greater than 20 kpc, which might be a remnant of past gravitational interactions that formed tidal debris and gaseous streams infalling back into the overall G1 potential well. Unfortunately, the arc-galaxy configuration under study does not cover lower impact parameters for testing this hypothesis, but future objects may permit more conclusive detections.

Online Content Methods, along with any additional Extended Data display items and Source Data, are available in the online version of the paper; references unique to these sections appear only in the online paper.

Received 21 July; accepted 14 November 2017.
Published online 31 January 2018.

1. Churchill, C. W. *et al.* Low- and high-ionization absorption properties of Mg II absorption-selected galaxies at intermediate redshifts. I. General properties. *Astrophys. J. Suppl. Ser.* **130,** 91–119 (2000).
2. Chen, H.-W. *et al.* An empirical characterization of extended cool gas around galaxies using Mg II absorption features. *Astrophys. J.* **714,** 1521–1541 (2010).
3. Nielsen, N. M., Churchill, C. W. & Kacprzak, G. G. MAGIICAT II. General characteristics of the Mg II absorbing circumgalactic medium. *Astrophys. J.* **776,** 115 (2013).
4. Chen, H.-W. in *Outskirts of Galaxies* (eds Knapen, J. *et al.*) 291–331 (Springer, 2017).
5. Tytler, D. *et al.* Metal absorption systems in spectra of pairs of QSOs: how absorbers cluster around QSOs and other absorbers. *Mon. Not. R. Astron. Soc.* **392,** 1539–1572 (2009).
6. Martin, C. L. *et al.* The size and origin of metal-enriched regions in the intergalactic medium from spectra of binary quasars. *Astrophys. J.* **721,** 174–192 (2010).
7. Hennawi, J. F. *et al.* Binary quasars in the Sloan Digital Sky Survey: evidence for excess clustering on small scales. *Astron. J.* **131,** 1–23 (2006).
8. Rauch, M., Sargent, W. L. W., Barlow, T. A. & Carswell, R. F. Small-scale structure at high redshift. III. The clumpiness of the intergalactic medium on subkiloparsec scales. *Astrophys. J.* **562,** 76–87 (2001).
9. Lopez, S., Ellison, S., D'Odorico, S. & Kim, T.-S. Clues to the nature of high-redshift O VI absorption systems from their lack of small-scale structure. *Astron. Astrophys.* **469,** 61–74 (2007).
10. Chen, H.-W. *et al.* Spatially resolved velocity maps of halo gas around two intermediate-redshift galaxies. *Mon. Not. R. Astron. Soc.* **438,** 1435–1450 (2014).
11. Rubin, K. H. R. *et al.* Andromeda's parachute: a bright quadruply lensed quasar at $z=2.377$. Preprint at https://arxiv.org/abs/1707.05873 (2017).
12. Kereš, D., Katz, N., Weinberg, D. H. & Davé, R. How do galaxies get their gas? *Mon. Not. R. Astron. Soc.* **363,** 2–28 (2005).
13. Muratov, A. L. *et al.* Gusty, gaseous flows of FIRE: galactic winds in cosmological simulations with explicit stellar feedback. *Mon. Not. R. Astron. Soc.* **454,** 2691–2713 (2015).
14. Bacon, R. *et al.* The MUSE second-generation VLT instrument. *Proc. SPIE* **7735,** 773508 (2010).
15. Wuyts, E. *et al.* A bright, spatially extended lensed galaxy at $z=1.7$ behind the cluster RCS2 032727–132623. *Astrophys. J.* **724,** 1182–1192 (2010).
16. Dahle, H. *et al.* Discovery of an exceptionally bright giant arc at $z=2.369$, gravitationally lensed by the Planck cluster PSZ1 G311.65–18.48. *Astron. Astrophys.* **590,** L4 (2016).
17. Rigby, J. R., Wuyts, E., Gladders, M. D., Sharon, K. & Becker, G. D. The physical conditions of a lensed star-forming galaxy at $z=1.7$. *Astrophys. J.* **732,** 59 (2011).
18. Rigby, J. R. *et al.* The Magellan Evolution of Galaxies Spectroscopic and Ultraviolet Reference Atlas (MEGaSaURA) I: the sample and the spectra. *Astrophys. J. Suppl. Ser.* (in the press).
19. Nielsen, N. M., Churchill, C. W., Kacprzak, G. G. & Murphy, M. T. MAGIICAT I. The Mg II absorber-galaxy catalog. *Astrophys. J.* **776,** 114 (2013).
20. Lopez, S. *et al.* Metal abundances in a damped Lyα system along two lines of sight at $z=0.93$. *Astrophys. J.* **626,** 767–775 (2005).
21. Ellison, S. L. An efficient technique for pre-selecting low-redshift damped Lyα systems. *Mon. Not. R. Astron. Soc.* **368,** 335–340 (2006).
22. Tumlinson, J. *et al.* The COS-Halos Survey: rationale, design, and a census of circumgalactic neutral hydrogen. *Astrophys. J.* **777,** 59 (2013).
23. Ho, S. H., Martin, C. L., Kacprzak, G. G. & Churchill, C. W. Quasars probing galaxies. I. Signatures of gas accretion at redshift approximately 0.2. *Astrophys. J.* **835,** 267 (2017).
24. Steidel, C. C. in *QSO Absorption Lines (*ed. Meylan, G.) 139–152 (Springer, 1995).
25. Charlton, J. C. & Churchill, C. W. Mg II absorbing galaxies: halos or disks? *Astrophys. J.* **465,** 631–645 (1996).
26. Bouché, N. *et al.* Physical properties of galactic winds using background quasars. *Mon. Not. R. Astron. Soc.* **426,** 801–815 (2012).
27. Kacprzak, G. G., Churchill, C. W. & Nielsen, N. M. Tracing outflows and accretion: a bimodal azimuthal dependence of Mg II absorption. *Astrophys. J.* **760,** L7 (2012).
28. Bordoloi, R., Lilly, S. J., Kacprzak, G. G. & Churchill, C. W. Modeling the distribution of Mg II absorbers around galaxies using background galaxies and quasars. *Astrophys. J.* **784,** 108 (2014).
29. Kacprzak, G. G. in *Gas Accretion onto Galaxies* (eds Fox, A. & Davé, R.) 145–165 (Springer, 2017).
30. Muratov, A. L. *et al.* Metal flows of the circumgalactic medium, and the metal budget in galactic haloes. *Mon. Not. R. Astron. Soc.* **468,** 4170–4188 (2017).

Acknowledgements This work has benefitted from discussions with A. Smette, N. Nielsen and G. Kacprzak. S.L. thanks the European Southern Observatory Scientific Visitor Selection Committee for supporting a research stay at the ESO headquarters in Santiago, where part of this work was done. S.L. has been supported by FONDECYT grant number 1140838. This work has also been partially supported by PFB-06 CATA. N.T. acknowledges support from CONICYT PAI/82140055.

Author Contributions S.L. conceived and led the project. S.L. and N.T. wrote the MUSE telescope-time proposal and designed the observations. L.F.B. and N.T. prepared the remote observations and L.F.B. reduced the MUSE data. S.L., N.T. and C.L. analysed the data, performed simulations and devised ways to produce and interpret the results. S.L. wrote the main codes. N.T. and I.P. performed the blind survey of galaxies in the field of view. K.S. performed the lens model and L.F.B. supervised the design of Fig. 1. M.B.B. and L.F.B. performed the photometric characterization of the absorbing galaxies, and S.L., C.L. and N.T. the analysis of their spectra. Ancillary data from MagE and HST were provided by J.R.R. and M.D.G. S.L. wrote the manuscript and produced the rest of the figures, with contribution from N.T. All co-authors provided critical feedback and helped to shape the manuscript.

Author Information Reprints and permissions information is available at www.nature.com/reprints. The authors declare no competing financial interests. Readers are welcome to comment on the online version of the paper. Publisher's note: Springer Nature remains neutral with regard to jurisdictional claims in published maps and institutional affiliations. Correspondence and requests for materials should be addressed to S.L. (slopez@das.uchile.cl).

Reviewer Information *Nature* thanks H.-W. Chen and the other anonymous reviewer(s) for their contribution to the peer review of this work.

METHODS

Observations and data reduction. The data were obtained with the MUSE integral-field spectrograph[14] mounted on the ESO Very Large Telescope. The 1′ field of view is sampled with 349 × 352 0.2″-wide spaxels. MUSE uses image slicers combined with an array of 24 identical spectrographs that provide nearly 100,000 spectra simultaneously. Our set-up provided a wavelength range of 4,650–9,300 Å at a resolving power $R = \lambda/\Delta\lambda$ of 2,000–4,000. Each spectral bin is 1.25-Å wide. The observations were carried out in 'service mode' during dark time, with thin cirrus or clear-sky conditions, airmass below 1.8 and seeing better than 0.8″. We obtained a total of 21 exposures of 700-s on-target each. The exposures were taken within 'observing blocks' of four exposures each. We applied a small dithering and 90° rotations between exposures to reject cosmic rays and minimize patterns of the slicers on the processed combined cube. We reduced all of the observations using the MUSE pipeline recipe v1.6.4 and ESO reflex v2.8.5. We analysed the quality of the individual exposures by measuring the seeing and transparency in the 'white' images. Owing to changes in the weather conditions during integrations, some of the exposures come from aborted observing blocks (but are otherwise 700-s long). We discarded five of them for having guiding errors, poor point spread function or obvious transparency problems. The remaining 16 exposures were combined into one final science datacube. The total on-target time was therefore 3.1 h. The sky subtraction was improved on this cube using the Zurich Atmospheric Purge (ZAP) algorithm[31]. The wavelength solution, corrected for the motion of the Earth around the Sun and converted to vacuum, was checked satisfactorily at the position of the brightest knot in the arc against our MagE spectrum[18]. The spectral resolution at the Mg II absorption lines is FWHM = 2.7 Å, corresponding to about 140 km s^{-1} (or $R = 2{,}100$).

In this work we adopt a flat ΛCDM cosmology with $\Omega_\Lambda = 0.7$, $\Omega_m = 0.3$ and $H_0 = 70$ km s^{-1} Mpc^{-1}.

Spaxel combination. Unlike quasars, the source we study is (a) extended and (b) inhomogeneous in flux given the resolved background galaxy and the inhomogeneous lensing magnifications (Extended Data Fig. 1). Therefore, the spectrum extraction must proceed using an ad hoc flux combination to assure independent flux measurements while maximizing the final signal-to-noise ratio per spectral pixel. To first approximation we tried polygons of constant signal-to-noise ratio[32], but decided not to use them because widely different areas complicate the interpretation of absorption against an extended source. Instead, we perform a 'minimum size' binning based on a fixed grid that was defined by the spatial sampling. Because the seeing profile is sampled with four 0.2″ spaxels (FWHM) we use 4 × 4 binning. This means that the centre of each binned spaxel lies at least one seeing FWHM from any other. Offsetting the grid by ±1 unbinned spaxel shows that the choice of zero-point does not affect the results of the analysis.

Spectral extraction. To extract individual one-dimensional spectra for each binned spaxel (or 'position') we applied weights $w_{ij} = f_{ij}/v_{ij}$, where f_{ij} and v_{ij} are respectively the calibrated object flux and variance of spaxel (i, j). This weight is a modified version of that used to combine spectra with different signal-to-noise ratios optimally[33]; it assumes a low detector read-out noise, in which case v_{ij} approximates the total number of counts. This gives higher weights to brighter spaxels and may introduce a complicated bias towards highly magnified spaxels. Because we are interested in a small spectral range we defined a subcube that contains wavelengths 5,100–6,000 Å. This range includes the Mg II doublet, the Fe II $\lambda = 2{,}382$ Å and Fe II $\lambda = 2{,}600$ Å transitions, and the Mg I $\lambda = 2{,}852$ Å transition at $z_{\rm abs} = 0.98$. Because the array of variances is noisy in the spectral direction, to avoid introducing noise carried by the spectral weights we choose a weight integrated in the spectral direction in a small featureless region blueward of the Mg II lines (the red side is compromised by a sky emission-line residual). Also, this weight does not penalize the absorption troughs.

Spaxel selection and Gaussian fits. To search for Mg II we first created a signal-to-noise ratio map by selecting binned spaxels on top of the arc and with signal-to-noise ratio above 3 blueward of the expected Mg II absorption. This selected a total of 56 positions, corresponding to a total projected area surveyed of around 600 kpc^2. At each selected position a spectrum was extracted and an automatic Gaussian fit applied to the spectral region corresponding to $z_{\rm G1} = 0.98235$. The Mg II $\lambda = 2{,}796$ Å, $\lambda = 2803$ Å doublet was fitted with two Gaussians with a tied wavelength ratio, free doublet ratio and fixed line width (corresponding to the instrument spectral resolution, FWHM = 2.7 Å). Each fit provides a rest-frame absorption strength of the $\lambda = 2{,}796$ Å transition (or rest-frame equivalent width 'W_0') and a redshift (or radial velocity v), along with their statistical errors (Extended Data Tables 1 and 2). Fixing the line width provides more robust fits, as expected, avoiding false positives in regions with low signal-to-noise ratio. It also assumes that the instrumental profile dominates the line profile. This assumption may not hold for all of the positions, in which case we estimate that a systematic error of approximately 0.05 Å would be introduced in W_0 (not included in Extended Data Tables 1 and 2).

In addition to the fits, synthetic line profiles were created for comparison with the data. When a fit failed or the significance was below 3σ, a 2σ upper limit was calculated using $\sigma_{W_0}(1+z) = {\rm FWHM}/\langle S/N \rangle$, where σ_{W_0} is the expected rest-frame 1σ error in the W_0 measurement and $\langle$S/N$\rangle$ is the average continuum signal-to-noise ratio near the line. The procedure delivers 18 significant Mg II detections, all to the northeast of the arc. Finally, to create the absorption-strength and velocity maps, the fitted W_0 and v values (or the W_0 upper limits) were recorded in images that had the same spatial sampling as the signal-to-noise ratio map.

We attempted simultaneous fits to the Fe II $\lambda = 2{,}382$ Å and Mg I $\lambda = 2{,}852$ Å transitions tied to the Mg II redshifts. (Unfortunately, the Fe II $\lambda = 2{,}600$ Å transition is blended with the C III] $\lambda = 1{,}907$ Å, $\lambda = 1{,}909$ Å emission-line doublet from the source galaxy[34] and therefore could not be fitted.) We detect significant Fe II at only three positions along the arc (Extended Data Table 3). These positions also show the strongest and most significant Mg II absorption. The corresponding Fe II/Mg II strength ratios lie in the rather narrow range of 0.5–0.7 and conform to the quasar statistics of very strong ($W_0 > 1$ Å) Mg II systems[35]. Non-detections do not constrain these ratios at other positions of the arc owing to either too weak Mg II or too low signal-to-noise ratio. Although the Fe II data are limited, the similar ratios tentatively hint at homogeneous enrichment along the arc. One of these positions shows a (marginal) Mg I detection.

The absorption signal in the maps, although significant, is expected to be weak and directly affected by the inhomogeneous signal-to-noise ratio. To rule out possible artefacts due to reduction or analysis effects, we conducted mock tests by simulating a flat W_0 distribution in a cube with the same signal-to-noise ratio per spaxel as the actual data. The outcome of these tests shows that our fitting procedure recovers a true signal in nearly 100% of the (binned) spaxels with a signal-to-noise ratio above 3, which justifies our signal-to-noise ratio cutoff.

Galaxies at $z = 0.98$. We searched systematically for galaxies in the MUSE cube near $z = 0.98$. The search included continuum sources and emission-line galaxies. We detected three [O II] sources, which we refer to as G1, G2 and G3 (Extended Data Fig. 2). These sources form a triangle with sides of 42″, 47″ and 64″, or $d = 231$ kpc, 259 kpc and 341 kpc in the absorber plane. G1 is resolved into three galaxies in the HST continuum images, which are barely resolved by MUSE. We refer to them as G1-A, G1-B and G1-C. From Gaussian fits to the [O II] $\lambda = 3{,}726$ Å, $\lambda = 3{,}729$ Å doublet in the MUSE spectra we obtained redshifts, line velocity dispersions, [O II] luminosities and star-formation rates for the five galaxies. The deconvolved velocity dispersions are subject to systematics, owing to the modest MUSE resolution. Assuming virial equilibrium, the velocities of G1, G2 and G3 lead to a virial radius $R_{\rm vir} < d$ and thus we do not consider them to be bound gravitationally, owing to their projected separations. Instead, we deem them to be three independent systems that lie in the same large-scale structure at $z = 0.98$.

G1-A, G1-B and G1-C represent our best absorbing-galaxy-system candidate, owing to their proximity to the place where the arc absorption occurs. The proximity of G1-A, G1-B and G1-C may cast doubts on whether they are indeed distinct galaxies, as opposed to a single disk in which dust obscuration would mimic the presence of different objects. But the fact that they are resolved also in the rest-frame I band (F160W) supports the existence of distinct galaxies.

We obtained the photometry from HST images in the F606W, F814W, F098M, F125W and F160W bands. We used SExtractor[36] in dual mode using the detections in the F160W band as a reference to obtain AB magnitudes in a 0.8″-diameter aperture. $B - I$ rest-frame colours were computed from F814W and F160W because these filters are the closest in effective wavelength. We used a local Scd galaxy spectral template[37] that well represents the colour of these galaxies to correct for any mismatch in the effective passbands. Small extinction corrections[38] were also applied. Using the multi-band photometry and a spectral energy distribution (SED) fitting code[39], we estimated luminosities, stellar masses and star-formation rates. These quantities are subject to large uncertainties owing to the use of just five passbands. We also computed star-formation rates for each galaxy from the [O II] line fluxes, integrated over 16 unbinned spaxels. These line fluxes are subject to extinction and therefore must be treated only as lower limits. Using Kennicutt's prescription[40], the emission-line luminosities translate into star-formation rates that are broadly consistent with those obtained from the SED fitting. These values were corrected for magnification μ by using our lens model. From the stellar masses we estimate dark-matter halo masses $M_{\rm h}$ using the prediction from abundance matching[41]. We then determine the corresponding virial radius using the relation $R_{\rm vir} = [3M_{\rm h}/(200\rho_{\rm c}4\pi)]^{1/3}$, where $\rho_{\rm c}$ is the critical density of the Universe at $z = 0.98$. The galaxy data are summarized in Extended Data Table 4.

Lens model. We base our lens model on a previous lensing analysis of this cluster[42]. We improve this previous lens model with new lensing constraints, including three new spectroscopic redshifts that we measured from the MUSE data. We obtain a spectroscopic redshift for the radial arc S7a/S7b in ref. 42 of $z_{\rm spec} = 2.82624$. We identify two new sets of lensed galaxies, at $z_{\rm spec} = 2.7$ and $z_{\rm spec} = 5.2$. Including more spectroscopic redshift constraints substantially reduces the lens model uncertainties and improves the accuracy[42,43]. The lens model is computed using the public software Lenstool[44], which uses a Markov chain Monte Carlo (MCMC) process to explore the parameter space. The lens model results in a computed projected mass density distribution in the lens plane, magnification maps for any given redshift, deflection fields, and their uncertainties. The deflection matrices are calculated using the lens equation, $\boldsymbol{\beta} = \boldsymbol{\theta} - (d_{\rm ls}/d_{\rm s})\boldsymbol{\alpha}(\boldsymbol{\theta})$, where $\boldsymbol{\beta}$ is the source position at $z_{\rm source}$, $\boldsymbol{\theta}$ is the observed position, $d_{\rm ls}$ and $d_{\rm s}$ are the distances from the lens to the source and from the observer to the source, respectively, and $\boldsymbol{\alpha}(\boldsymbol{\theta})$ is the deflection angle at the observed position. We note that any plane behind the lens can be considered the source plane, and this equation also applies to the absorber plane.

To assess the completeness of our search for [O II] in emission, we scanned the magnification map near Mg II looking for regions with much lower magnification than on top of G1 and G2. We found none, indicating that these galaxies are not sitting on particularly highly magnified regions; consequently, we are confident that our absorber candidates are robust and no other galaxies (of similar brightness but non-magnified) were missed from our search.

Spatial resolution and impact parameters. We use the deflection matrices to de-lens the coordinates of our binned spaxels into the absorber plane and to calculate impact parameters. Extended Data Fig. 3 shows a de-lensed image of the arc projected against the image plane. Owing to the inhomogeneous lensing deflection, when the spaxels are traced from the image plane to the absorber plane the shape of the binned spaxels changes in the absorber plane, although there is no overlap between them. Assuming that the light rays do not intercept each other after being absorbed, our signal should probe independent areas of the absorber. We discuss the unequal spaxel areas below.

From Extended Data Fig. 3 it is also evident that although the angular resolution is constant across the image plane, the actual spatial resolution—defined in the absorber plane—is not. To define an ad hoc 'spatial resolution' we take the square root of the area of each de-lensed spaxel. We find that this number ranges from around 4 kpc at the east side of the arc to around 2 kpc at the western side.

To calculate impact parameters we multiply the de-lensed angular separations between spaxels and G1 by the scale at $z = 0.98$ given by the adopted cosmology, 7.97 kpc per arcsecond. From a large set of MCMC realizations, we estimate the statistical 1σ uncertainty associated with the angular separations to be less than about 2%. Including model systematics[43], impact parameters should be precise to less than about 5% for the assumed cosmology.

Partial covering. The background source is likely to be more extended than the typical size of the absorbing clouds, leading to possible partial covering[45]. To test this effect on our signal we performed a second run of automatic Mg II fits on a 8×8 spaxel map. Extended Data Fig. 4 shows the cumulative distributions of W_0 and v for the 4×4 and 8×8 binnings. The stronger binning indeed skews the W_0 distribution to lower values. This is probably due to averaging arc light without Mg II absorption; although, given the arc geometry, at this spaxel size (1.6″) we also expect some sky contamination (not so in the 4×4 binning). Conversely, the velocity distribution remains unaffected. We conclude that (a) the chosen 4×4 binning is our best option above the seeing limitation; and (b) we cannot exclude a level of partial covering in our W_0 sample, although such an effect is not affecting the absorption velocities.

Particularly relevant to interpreting our results, the physical areas covered by the binned spaxels are unequal in the absorber plane (Extended Data Fig. 3). These areas are of the order of 10 kpc^2, at least 10^7 times larger than those probed by the quasar beams (less than about 1 pc). Clearly, our arc measurements sample an average signal at each position. Therefore, measurements at different positions are comparable with each other and, to a great extent, also independent of the spaxel area. The only effect of having uneven areas in the absorber plane should be on the intrinsic scatter of each measurement, with smaller spaxels having more scatter. We cannot measure this intrinsic scatter, but consider its effect to be negligible given that the goal is to make a comparison with measurements obtained along the much narrower quasar beams.

Gas covering fractions. To calculate gas covering fractions we compute the fraction of positions with positive detections above a given W_0 cutoff, $W_{\rm cut}$, in a given impact parameter (D) range. Non-detections are accounted for by considering only (2σ) upper limits below $W_{\rm cut}$. We select $W_{\rm cut}$ and ranges of D to enable comparisons with two quasar-absorber statistics.

To compare with the survey presented in ref. 2, we assume an average galaxy magnitude $\langle M_{\rm B}\rangle = -19.0$ and use $W_{\rm cut} = 0.5$ Å. We find covering fractions of 100% (2/2; in the range 16 kpc $< D <$ 20 kpc), 80% (4/5; 20 kpc $< D <$ 25 kpc) and 38% (6/16; 25 kpc $< D <$ 39 kpc). The quasar statistics for low-luminosity galaxies gives[2] 60%, 20% and 0%, respectively, for the three ranges of D. These figures suggest that the covering fraction of the intervening gas is larger towards this arc than towards the quasars in that sample.

On the other hand, to compare with the survey presented in ref. 3, we use two cut-offs: $W_{\rm cut} = 0.6$ Å and $W_{\rm cut} = 1.0$ Å. For $W_{\rm cut} = 0.6$ Å we find covering fractions of 67% (6/9; 0 kpc $< D <$ 25 kpc), and 20% (4/20; 25 kpc $< D <$ 50 kpc). The quasar statistics for low-luminosity galaxies ($0.07 < L_{\rm B}/L^*_{\rm B} < 0.94$, where L^* is the characteristic luminosity of galaxies and B denotes the rest-frame B band) gives[3] 71% and 48%, respectively. For $W_{\rm cut} = 1.0$ Å we find covering fractions of 18% (2/11) and 4% (1/26), respectively, for the same ranges of D. The quasar statistics gives 29% and 24%. Therefore, for both W_0 cut-offs, the covering fractions for the arc are smaller than those for the quasars in this sample.

Finally, we note that these comparisons are subject to uncertainties because we do not cover exactly the same impact-parameter ranges.

Code availability. This analysis is based on custom Python routines, some of which use the MUSE Python data analysis framework[46] and the open-source plotting package for Python APLpy[47]. We have opted not to make our routines available because they are described in detail in the paper.

Data availability. The observations discussed in this paper were made using European Southern Observatory (ESO) Telescopes at the La Silla Paranal Observatory under programme ID 098A.0459(A). The corresponding data are available on the ESO archive at http://archive.eso.org/cms.html.

31. Soto, K. T., Lilly, S. J., Bacon, R., Richard, J. & Conseil, S. ZAP – enhanced PCA sky subtraction for integral field spectroscopy. *Mon. Not. R. Astron. Soc.* **458,** 3210–3220 (2016).
32. Cappellari, M. & Copin, Y. Adaptive spatial binning of integral-field spectroscopic data using Voronoi tessellations. *Mon. Not. R. Astron. Soc.* **342,** 345–354 (2003).
33. Robertson, J. G. Optimal extraction of single-object spectra from observations with two-dimensional detectors. *Publ. Astron. Soc. Pacif.* **98,** 1220–1231 (1986).
34. Rigby, J. R. *et al.* C III emission in star-forming galaxies near and far. *Astrophys. J. Lett.* **814,** L6 (2015).
35. Rodríguez Hidalgo, P. *et al.* Evolution of the population of very strong Mg II absorbers. *Mon. Not. R. Astron. Soc.* **427,** 1801–1815 (2012).
36. Bertin, E. & Arnouts, S. SExtractor: software for source extraction. *Astron. Astrophys. Suppl. Ser.* **117,** 393–404 (1996).
37. Coleman, G. D., Wu, C.-C. & Weedman, D. W. Colors and magnitudes predicted for high redshift galaxies. *Astrophys. J. Suppl. Ser.* **43,** 393–416 (1980).
38. Schlegel, D. J., Finkbeiner, D. P. & Davis, M. Maps of dust infrared emission for use in estimation of reddening and cosmic microwave background radiation foregrounds. *Astrophys. J.* **500,** 525–553 (1998).
39. Moustakas, J. *et al.* PRIMUS: constraints on star formation quenching and galaxy merging, and the evolution of the stellar mass function from $z = 0$–1. *Astrophys. J.* **767,** 50 (2013).
40. Kennicutt, R. C. Jr. Star formation in galaxies along the Hubble sequence. *Annu. Rev. Astron. Astrophys.* **36,** 189–231 (1998).
41. Moster, B. P. *et al.* Constraints on the relationship between stellar mass and halo mass at low and high redshift. *Astrophys. J.* **710,** 903–923 (2010).
42. Sharon, K. *et al.* Source-plane reconstruction of the bright lensed galaxy RCSGA 032727–132609. *Astrophys. J.* **746,** 161 (2012).
43. Johnson, T. L. & Sharon, K. The systematics of strong lens modeling quantified: the effects of constraint selection and redshift information on magnification, mass, and multiple image predictability. *Astrophys. J.* **832,** 82 (2016).
44. Jullo, E. *et al.* A Bayesian approach to strong lensing modelling of galaxy clusters. *New J. Phys.* **9,** 447 (2007).
45. Bergeron, J. & Boissé, P. Extent and structure of intervening absorbers from absorption lines redshifted on quasar emission lines. *Astron. Astrophys.* **604,** A37 (2017).
46. Bacon, R., Piqueras, L., Conseil, S., Richard, J. & Shepherd, M. MPDAF: MUSE Python data analysis framework. *Astrophysics Source Code Library* (2016).
47. Robitaille, T. & Bressert, E. APLpy: astronomical plotting library in Python. *Astrophysics Source Code Library* (2012).
48. Willmer, C. N. A. *et al.* The Deep Evolutionary Exploratory Probe 2 galaxy redshift survey: the galaxy luminosity function to $z \sim 1$. *Astrophys. J.* **647,** 853–873 (2006).

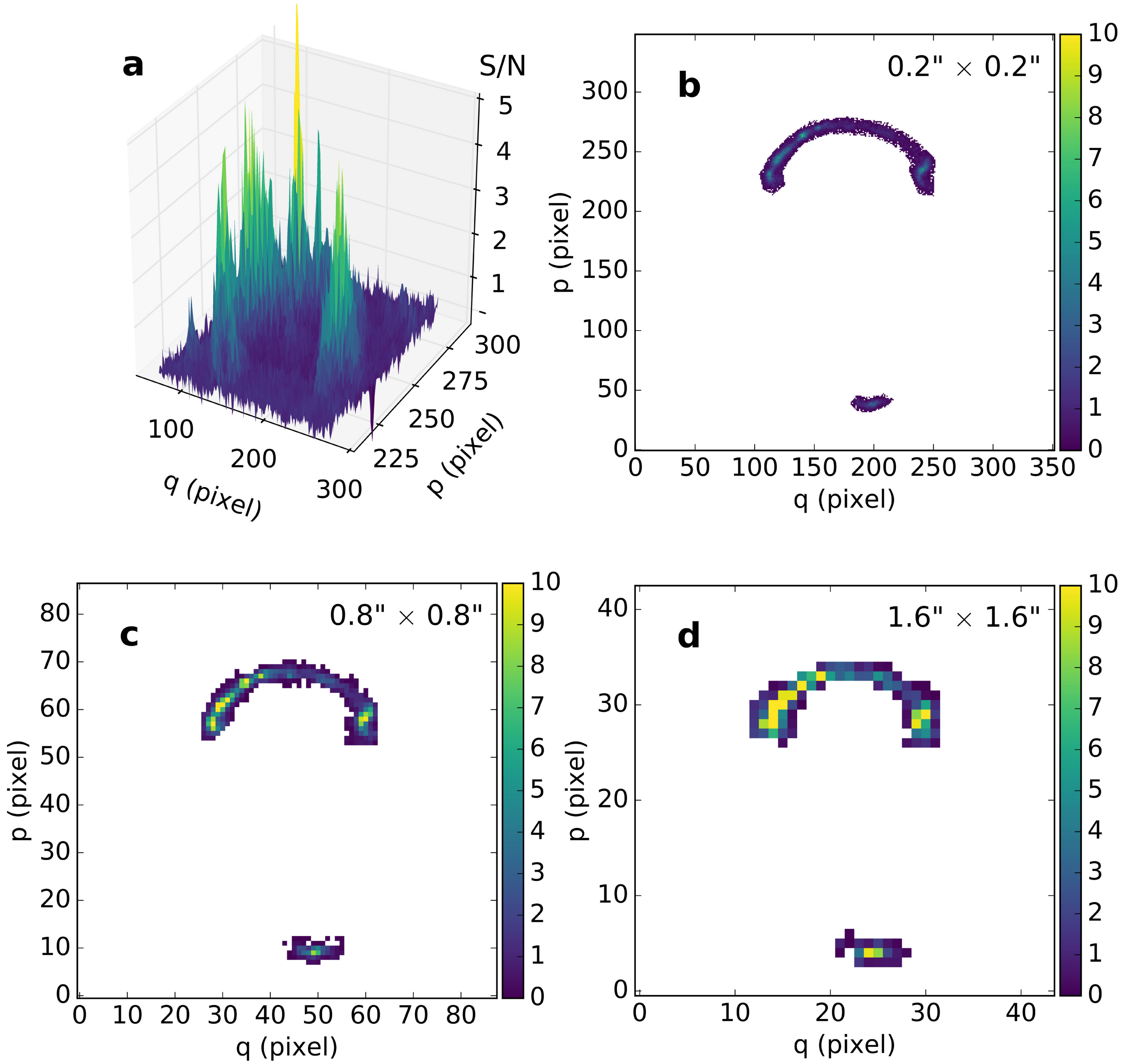

Extended Data Figure 1 | Signal-to-noise ratio versus binning. **a**, Three-dimensional representation of the signal-to-noise ratio (S/N) at the position of Mg II absorption in the unbinned data. **b**–**d**, Same as **a** but in two dimensions and for different binnings. The size of each binned spaxel is indicated in arcseconds; the colour scale is the same for all three panels. Note the expected increase in signal-to-noise ratio with binning size.

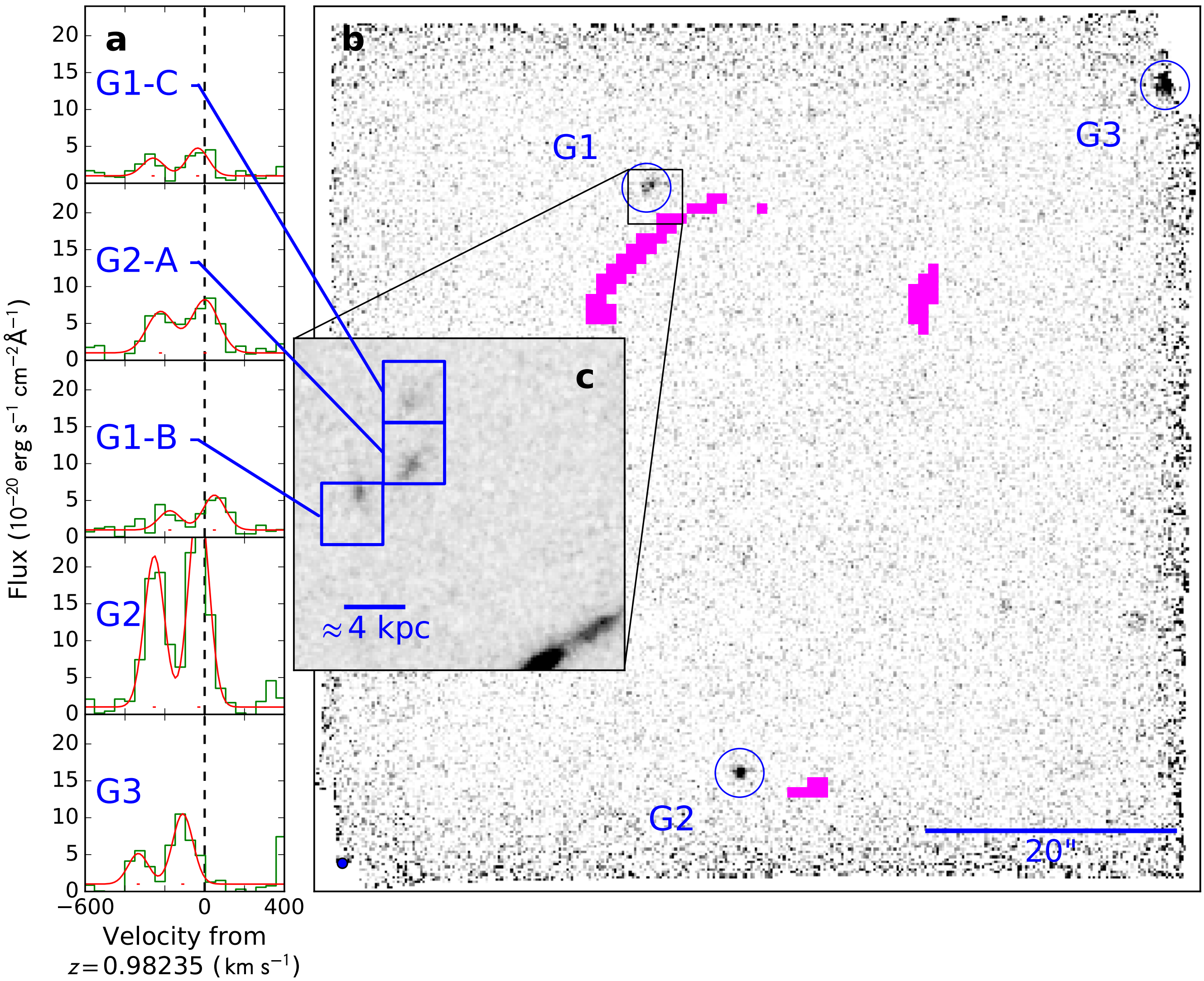

Extended Data Figure 2 | Emission-line galaxies at $z = 0.98$. **a**, Gaussian fits to the [O II] $\lambda = 3{,}726$ Å, $\lambda = 3{,}729$ Å doublets in the MUSE spectra of G1, G2 and G3, the three [O II] sources found by our systematic search. The MUSE spatial resolution barely resolves G1 into three [O II] clumps (G1-A, G1-B and G1-C), which cluster around $z_{G1} = 0.98235$ and have a velocity dispersion of 35 km s^{-1}. **b**, MUSE image of RCSGA 032727−132623 centred on [O II] emission at $z = 0.98$. The magenta squares indicate the binned spaxels used to map the Mg II absorption against the arc. **c**, HST/WFC3 F814W image zooming into the G1 system. The blue squares indicate the MUSE regions used to extract the [O II] spectra. The scale corresponds to the region close to G1 in the absorber plane.

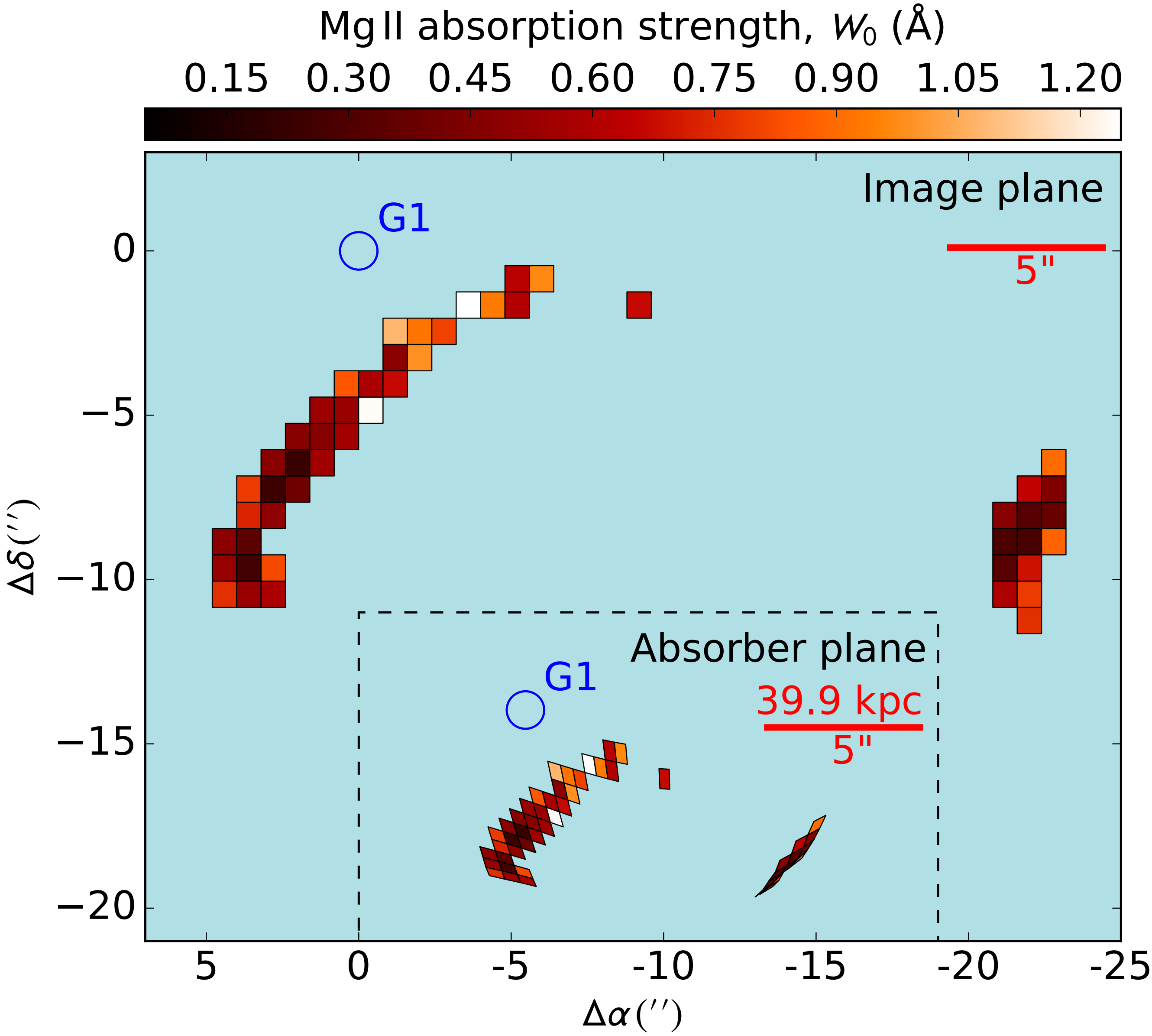

Extended Data Figure 3 | Projection of absorber plane against image plane. In the absorber plane (dashed rectangle), the spaxel configuration appears shrunked and the de-lensed spatial elements have different shapes and areas across the absorber plane. After de-lensing, the scale in the absorber plane is given by the adopted cosmology: $5'' = 39.85$ kpc at $z = 0.98$. The impact parameter used here is defined as the projected physical distance between a given position and G1 on this plane. For reference, a 5″ scale bar is shown in the image plane. Coordinates (α, right ascension; δ, declination) are in arcseconds relative to the position of G1 in the image plane.

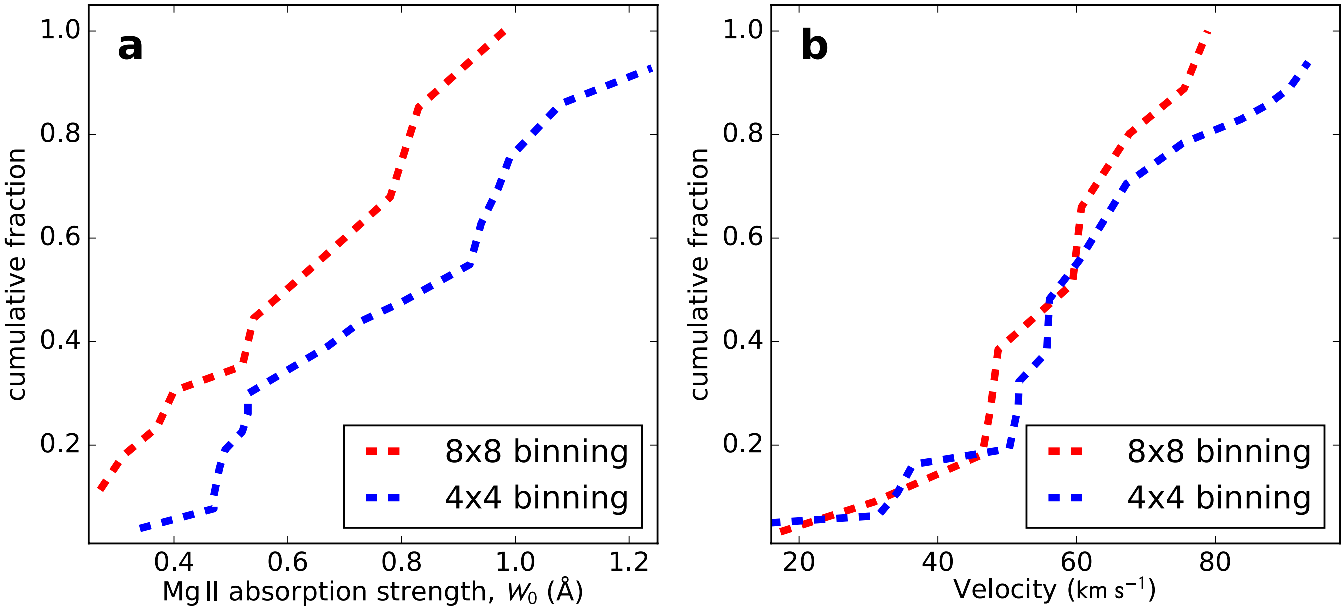

Extended Data Figure 4 | Effect of partial covering. a, Cumulative distribution of absorption strengths for two different binnings. **b**, Same as **a** but for velocities.

Extended Data Table 1 | Mg II absorption near G1

$\Delta\alpha$* ($''$)	$\Delta\delta$* ($''$)	D† (kpc)	W_0‡ (Å)	v§ (km s^{-1})	S/N‖
−22.0	−11.2	77.5	< 0.76	…	3.6
4.4	−10.4	40.3	< 0.76	…	3.6
3.6	−10.4	40.5	0.53 ± 0.14	55.7 ± 13.8	8.7
2.8	−10.4	41.3	< 0.59	…	4.6
−21.2	−10.4	76.5	< 0.60	…	4.5
−22.0	−10.4	78.0	< 0.79	…	3.4
4.4	−9.6	38.3	0.52 ± 0.18	15.7 ± 26.3	6.8
3.6	−9.6	38.5	< 0.26	…	10.6
2.8	−9.6	39.2	< 0.82	…	3.3
−21.2	−9.6	77.2	< 0.33	…	8.1
−22.0	−9.6	78.4	< 0.69	…	3.9
4.4	−8.8	36.2	< 0.49	…	5.5
3.6	−8.8	36.2	0.34 ± 0.12	50.3 ± 15.8	8.7
−21.2	−8.8	77.7	< 0.29	…	9.2
−22.0	−8.8	79.5	< 0.28	…	9.8
−22.8	−8.8	81.1	< 0.88	…	3.1
3.6	−8.0	33.8	0.73 ± 0.24	60.4 ± 25.0	5.1
2.8	−8.0	34.3	< 0.50	…	5.4
−21.2	−8.0	77.8	< 0.48	…	5.6
−22.0	−8.0	79.9	< 0.32	…	8.5
−22.8	−8.0	81.8	< 0.38	…	7.1
3.6	−7.2	31.2	< 0.79	…	3.5
2.8	−7.2	31.5	< 0.24	…	11.3
2.0	−7.2	32.6	< 0.40	…	6.8
−22.0	−7.2	80.1	< 0.65	…	4.2
−22.8	−7.2	82.4	< 0.45	…	6.1
2.8	−6.4	28.6	0.48 ± 0.17	34.2 ± 23.5	9.8
2.0	−6.4	29.5	< 0.23	…	12.1
1.2	−6.4	30.7	< 0.56	…	4.8
−22.8	−6.4	82.8	< 0.90	…	3.0
2.0	−5.6	26.3	0.47 ± 0.14	93.4 ± 25.9	7.4
1.2	−5.6	27.4	0.47 ± 0.10	51.7 ± 18.0	10.6
0.4	−5.6	28.9	< 0.56	…	4.9
1.2	−4.8	23.8	< 0.54	…	5.1
0.4	−4.8	25.2	0.53 ± 0.12	63.5 ± 12.3	7.2
−0.4	−4.8	27.1	1.24 ± 0.43	115.4 ± 29.0	3.2
0.4	−4.0	21.4	< 0.85	…	3.2
−0.4	−4.0	23.2	< 0.59	…	4.6
−1.2	−4.0	25.4	0.67 ± 0.26	83.7 ± 16.1	3.2
−1.2	−3.2	21.3	0.49 ± 0.11	75.3 ± 9.9	7.9
−2.0	−3.2	23.8	0.99 ± 0.15	90.7 ± 9.7	8.3
−1.2	−2.4	17.1	1.08 ± 0.19	87.5 ± 12.6	7.8
−2.0	−2.4	19.7	0.92 ± 0.11	51.6 ± 7.3	11.0
−2.8	−2.4	22.4	0.80 ± 0.24	31.4 ± 19.0	5.2
−3.6	−1.6	21.7	1.42 ± 0.20	36.4 ± 11.3	5.0
−4.4	−1.6	24.7	0.94 ± 0.14	56.1 ± 9.2	9.0
−5.2	−1.6	27.3	< 0.61	…	4.5
−9.2	−1.6	40.6	< 0.67	…	4.1
−5.2	−0.8	24.5	< 0.63	…	4.3
−6.0	−0.8	27.6	0.97 ± 0.26	67.2 ± 17.5	3.4

*Arc-position angular separation to G1 in the image plane.
†Projected physical separation to G1 in the absorber plane.
‡Mg II $\lambda = 2{,}796$ Å absorption strength (with 1σ error) or 2σ upper limit.
§Velocity relative to $z_{G1} = 0.98235$.
‖Signal-to-noise ratio blueward of Mg II.

Extended Data Table 2 | Upper limits on Mg II absorption near G2

$\Delta\alpha^*$ (″)	$\Delta\delta^*$ (″)	$D^\dagger$ (kpc)	$W_0^\ddagger$ (Å)	$v^\S$ (km s^{-1})	S/N$^{\|\|}$
−4.2	−1.6	22.0	< 0.81	...	3.4
−5.0	−1.6	25.2	< 0.70	...	3.9
−5.8	−1.6	28.9	< 0.32	...	8.6
−6.6	−1.6	32.5	< 0.41	...	6.7
−5.8	−0.8	27.1	< 0.79	...	3.4
−6.6	−0.8	30.9	< 0.60	...	4.5

*Arc-position angular separation to G2 in the image plane.
†Projected physical separation to G2 in the absorber plane.
‡Mg II $\lambda = 2{,}796$ Å absorption strength 2σ upper limit.
§Velocity relative to $z_{G1} = 0.98235$.
||Signal-to-noise ratio blueward of Mg II.

Extended Data Table 3 | Absorption by Fe II and Mg I near G1

$\Delta\alpha$ ($''$)	$\Delta\delta$ ($''$)	D (kpc)	W_0^{2796} (Å)	W_0^{2382} (Å)	W_0^{2852} (Å)
−2.0	−3.2	23.8	0.99 ± 0.15	0.72 ± 0.22	< 0.35
−1.2	−2.4	17.1	1.08 ± 0.19	0.59 ± 0.21	0.44 ± 0.15
−4.4	−1.6	24.7	0.94 ± 0.14	0.62 ± 0.19	< 0.31

Extended Data Table 4 | Galaxy properties

ID	RA (deg)	DEC (deg)	z	v (km s^{-1})	$\Delta v_{\rm FWHM}$ (km s^{-1})	$m_{\rm F814W}$ (AB)	B-I
(1)	(2)	(3)	(4)	(5)	(6)	(7)	(8)
G1−A	51.867229	−13.434300	0.98236	$+1.8 \pm 7.0$	138.0 ± 10.4	24.30 ± 0.03	0.68 ± 0.03
G1−B	51.867420	−13.434390	0.98267	$+48.8 \pm 12.0$	97.9 ± 18.4	24.64 ± 0.04	0.53 ± 0.04
G1−C	51.867229	−13.434060	0.98212	-35.2 ± 12.5	92.5 ± 17.9	24.85 ± 0.05	0.72 ± 0.05
G2	51.865139	−13.447130	0.98216	-29.2 ± 1.7	81.0 ± 2.8	24.27 ± 0.03	0.06 ± 0.03
G3	51.855511	−13.431970	0.98162	-109.8 ± 12.2	86.9 ± 17.4	23.99 ± 0.02	0.30 ± 0.02
ID	M_B	L/L^*	$\log M_*/M_\odot$	$f_{\rm OII}$ (erg s^{-1} cm^{-2})	SFR ($M_\odot$ yr^{-1})	μ	$R_{\rm vir}$ (kpc)
(1)	(2)	(3)	(4)	(5)	(6)	(7)	(8)
G1−A	−18.37	0.05	9.5	$8.7 \cdot 10^{-18}$	0.23	2.6	92
G1−B	−17.92	0.03	9.1	$4.0 \cdot 10^{-18}$	0.11	2.7	79
G1−C	−17.81	0.03	9.1	$3.3 \cdot 10^{-18}$	0.09	2.5	79
G2	−18.86	0.08	9.0	$2.4 \cdot 10^{-17}$	0.85	2.0	73
G3	−19.08	0.10	9.4	$6.9 \cdot 10^{-18}$	0.28	1.7	85

Top row: columns (1)–(3) galaxy identification (ID) and coordinates (RA, right ascension; DEC, declination); (4) redshift (z); (5) velocity relative to $z_{\rm G1} = 0.98235$ (v); (6) deconvolved [O II] line width ($\Delta v_{\rm FWHM}$); (7) apparent magnitude ($m_{\rm F814W}$); (8) rest-frame colour ($B - I$). Bottom row: column (2) absolute magnitude (M_B); (3) rest-frame B-band luminosity in terms of L^* at $z = 0.98$ (L/L^*; ref. 48); (4) stellar mass ($\log(M_*/M_\odot)$; from SED fitting); (5) [O II] emission line flux ($f_{\rm OII}$); (6) star-formation rate (SFR; from emission line flux); (7) magnification (μ; subject to approximately 5% uncertainty); (8) virial radius ($R_{\rm vir}$). Magnification was used to correct quantities in columns (2)–(6) in the bottom row.